

Intelligent optoelectronic processor for orbital angular momentum spectrum measurement

Hao Wang¹, Ziyu Zhan¹, Futai Hu¹, Yuan Meng¹, Zeqi Liu¹, Xing Fu^{1,2} and Qiang Liu^{1,2}

¹State Key Laboratory of Precision Measurement of Technology and Instruments, Department of Precision Instrument, Tsinghua University, Beijing 100084, China

²Key Laboratory of Photonic Control Technology, Ministry of Education, Beijing 100084, China

These authors contributed equally: Hao Wang, Ziyu Zhan

Correspondence: Xing Fu (fuxing@tsinghua.edu.cn), Qiang Liu (qiangliu@tsinghua.edu.cn)

Abstract

Structured light carrying orbital angular momentum (OAM) has propelled the advancement of massive fundamental discoveries and applications such as communication and quantum analogy, thereby posing increasing demands on its effective detection schemes. Conventional schemes based on e.g. phase retrieval are troubled with low speed, complicated system, poor robustness, etc. Here, we devise an intelligent processor composed of photonic and electronic neurons for measuring the OAM spectrum in an accurate, fast and direct manner. Specifically, cascaded optical layers extract invisible topological charge (TC) information from incoming light and a shallow electronic layer predicts the exact OAM spectrum. Compared with existing alternatives, the integration of optical-computing in the system promises us a compact single-shot measurement scheme with high detection speed and energy efficiency (optical operations / electronic operations $\sim 10^3$), neither necessitating reference wave nor repetitive steps. Results show our processor is endowed with salient generalization ability and robustness against diverse structured light and adverse effects. Besides, it exhibits exceptional performance (mean squared error $\sim 10^{-5}$) on unseen experimental data though trained on a fully simulated dataset, which sharply eases the workload on collecting massive labelled experimental training set. We further raise a model interpretation paradigm to reveal the underlying physical mechanisms in hybrid deep learning system, in distinct to conventional black-box neural networks. Our work not only contributes to the explorations on OAM physics and applications, and also broadly inspires the advanced link between intelligent computing and physical effects.

Introduction

Vortex beams are proved to carry orbital angular momentum (OAM) as a new degree of freedom in addition to polarization and wavelength¹. All OAM states of light constitute a Hilbert space, providing a new avenue to high-capacity communications², micro-manipulation³, and quantum information processing⁴. Precise and efficient detection of OAM distribution consequently becomes a pivotal demand for these promising applications. We note the OAM spectrum, which reflects the relative power distribution of certain structured light on eigenmode bases, is a universal metric. Several previously proposed detection methods such as interferometry⁵, diffractometry⁶, and coordinate transformation^{7, 8} are suitable for only detecting the existence of OAM but fail to extract an exact power distribution of OAM states. To this end, schemes based on mode projection and phase retrieval are explored⁹⁻¹¹, yet requiring not only many repetitive steps in data acquiring and postprocessing but also strict experimental calibration. Rotational Doppler effect is also employed to construct an OAM complex spectrum analyzer¹², at the cost of complicated detection setup

and low speed. Another sequential weak and strong measurements in single-photon scenarios successfully reconstructs complex probability of 27-dimensional OAM states¹³ but still fall short in terms of system conciseness and working speed. In short, despite of these realizations⁵⁻¹⁴, the limitations of detection speed, accuracy, range, robustness, generalization ability, and system conciseness hinder their practicability towards stable, fast and accurate information transfer in the modern age.

Along with enduring efforts in vortex beams comes the development of artificial intelligence (AI). In particular, deep learning (DL)¹⁵, has gradually revolutionized wide-ranging disciplines such as genetics¹⁶, biomedical diagnosis¹⁷ and physics¹⁸. In optics, data-driven deep learning algorithms are becoming pervasive tools to augment performance and to infuse new functionalities in super-resolution microscopy¹⁹, 3D holography²⁰, ultrafast photonics²¹, optical components design²², optical metrology²³, etc. Recently, DL algorithms are also introduced to recognize OAM modes²⁴⁻²⁷ due to their inherent ability to analyze complex patterns²⁸. However, the distinguishment of degenerate intensities patterns carrying different OAM spectra become a major challenge. More importantly, previous DL-related endeavors often face poor generalization ability and heavy electronic computational consumption.

What follows the flourishing of DL is the inconceivable demands for computing hardware, especially at the era of big data. The computing power required to train or execute state-of-the-art DL models increases vastly while people's expectation on faster computing speed is still high. On the other hand, the development of integrated electronic circuits is levelling out, unable to keep pace with the well-known Moore's law. Owing to the advantages of low latency, high energy efficiency and high parallelism, photonics thus establishes itself in a central position when the computation community is seeking alternative technologies for continued performance improvements²⁹⁻³¹. Many seminal photonic computing schemes are proposed recently³²⁻³⁶. Among them, wave-optics-based Diffractive Deep Neural Network (D²NN) distinguishes itself with great flexibility³³, depth advantage³⁷, and scalability³⁸. In addition to many machine-vision demonstrations^{33, 38}, it has been successfully incorporated into the diffuser imaging system³⁹, pulse shaping system⁴⁰, optical logic operation system⁴¹, along with extension to different wavelengths⁴²⁻⁴⁵.

Here, we demonstrate a single-shot measurement scheme called POAMS (processor for OAM spectrum) with high speed and robustness, leveraging a hybrid optoelectronic neural network (Fig. 1). An optical diffractive network is synergized with a shallow electronic readout layer to predict the exact OAM spectrum for incoming structured light in a regressive manner. The obtained results on unknown experimental single and multiplexed modes show that POAMS could be an optimal solution to the OAM detection issue compared with the most advanced alternatives (see Supplementary Table S1 for comparison details), featuring several critical properties: 1) high speed and energy efficiency: it works at microsecond level with most computation operations (~ 99.98% of all operations) optically conducted which cost little to no energy; 2) high accuracy: it can reconstruct sophisticated even random relative weights with mean squared error (MSE) around $10^{-5} \sim 10^{-3}$; 3) conciseness: it entails neither reference wave nor repetitive measurements with a system size of $\sim 100\lambda \times 100\lambda \times 200\lambda$; 4) high robustness: it exhibits successful results even in the presence of adverse effects such as atmosphere turbulence, misalignment, and rotation without any adaptive optics compensation techniques; 5) great generalization ability: it functions well on experimental modes with diverse OAM spectra but without necessitating massive experimental training set; 6) great extendibility: it is implanted onto directly calculating OAM complex spectrum (i.e. the relative power and phase distribution). Moreover, we propose a model interpretation/visualization paradigm to comprehend

the underlying physical mechanisms of our hybrid DL processor thus removing the “black-box” nature of neural networks. The optical part accounts for complex optical field sensing/processing, while the electronic part is responsible for real signal processing or final regression. The synergy of both parts promises us a powerful and concise platform to facilitate OAM-based high speed information processing and to explore new opportunities and mechanisms of hybrid optoelectronic neural networks.

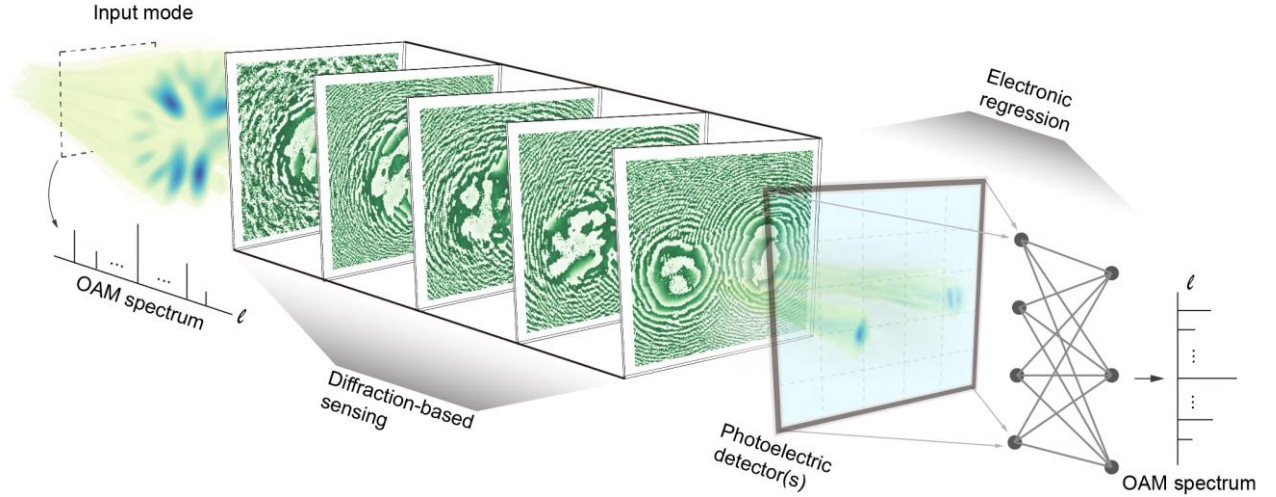


Fig. 1 Illustration of the hybrid processor for OAM spectrum measurement. The incident structured mode with certain OAM distribution is firstly processed by the diffractive optical neural network, whereby the topological information is transformed into high-dimensional sparse feature in the photoelectric detector plane. In this case, the optical diffraction-based sensing part can ‘split’ the input beam into two main lobes that are related to positive and negative topological charges respectively. Once the complex optical field is turned into real-numbered intensity patterns through the detector, the shallow fully connected layer can recover the OAM spectrum in a regressive manner (see detailed forward and backward model in Methods).

Results

Processor for OAM spectrum. Any general structured light $E(\rho, \theta, z)$ can be fully characterized by spatially mathematically decomposing it onto orthogonal vortex modes:

$$E(\rho, \theta, z) = \sum_{\ell=K_N}^{K_P} c_\ell \exp(i\ell\theta), \quad (1)$$

where (ρ, θ, z) are cylindrical coordinates, K_P and K_N denote positive and negative OAM spectrum bounds for a given detection scenario (normally $|K_P| = |K_N|$ and they could be infinite), and $c_\ell = a_\ell \exp(i\phi_\ell)$ represents complex coefficient with respect to certain mode component. For brevity, here we normalize the amplitude a_ℓ as $\sum_{\ell=K_N}^{K_P} |a_\ell|^2 = 1$ and ϕ_ℓ indicates intermodal phase with respect to a global reference phase. The OAM spectrum that elucidates the relative power distribution of all components can thus be expressed as a vector $s = [|a_{K_N}|^2, |a_{K_N+1}|^2, \dots, |a_{K_P}|^2]$. Calculating s from a given structured light is generally not easy and can be treated as an inverse problem. Figure 1 illustrates the workflow of our system to retrieve the OAM spectrum \hat{s} . Accordingly, the whole picture of information processing in our scheme can be expressed as:

$$\hat{\mathbf{s}} = \mathcal{F}_E \left(\mathcal{F}_N \left(\mathcal{F}_O (E(\rho, \theta, z)) \right) \right), \quad (2)$$

with \mathcal{F}_E and \mathcal{F}_O the electronic regression function and the optical diffraction-based wavefront sensing function respectively, and \mathcal{F}_N the natural quadratic (nonlinear) function brought by photoelectric effect of a sensor. The optical neural network is composed of five cascaded phased layers with fixed distance and each layer is endowed with 200^2 programmable nodes (neurons). They serve as a special mapping to project the incident complex optical wave into a latent space once trained. The transformed complex features in the latent space are switched to measurable real-numbered currents by the photoelectric sensor. Then the compressed real features are fed into the shallow electronic fully connected layer (FCL) to obtain the spectrum (detailed in Methods section). Note that earlier approaches involving all-optical D²NN or hybrid D²NN are normally applied for classification tasks in machine vision such as MNIST database^{33, 46}. The POAMS in this work is distinctive from previous endeavors due to its powerful *regression* behavior with respect to *eigen solutions* of the Helmholtz equation, as we will discuss below. Notably, when an optical wave with certain OAM distribution enters the framework (Fig. 1), it is processed naturally as it propagates forwards, interacts with the passive phase layers and gets transformed into the spectrum without any other references, manifesting a single-shot measurement.

Results and analysis. The proposed system architecture is shown in Fig. 1, where we craft the OAM spectrum analyzer during iteratively training with error backpropagation technique. The objective function can be expressed as:

$$\min_{\theta_o, \theta_E} \mathcal{L}(\mathbf{s}, \hat{\mathbf{s}}; \theta_o, \theta_E) + \mathcal{C} \|\theta_o\|_2^2 + \mathcal{C} \|\theta_E\|_2^2, \quad (3)$$

where $\mathcal{L}(\mathbf{s}, \hat{\mathbf{s}}; \theta_o, \theta_E)$ refers to the loss function comparing the processor's output $\hat{\mathbf{s}}$ and ground truth \mathbf{s} , and θ_o, θ_E are optical and electronic neurons. Though parameters θ_o and θ_E are updated simultaneously, they are not balanced initially. We introduce two more hyperparameters (see Methods) and fine tuning them leads to the smooth convergence of the hybrid model as shown in Fig. 2a. The latter two terms with constant \mathcal{C} , known as L_2 regularization, are added as penalties to prevent overfitting and increase model sparsity.

The two adjacent loss curves in Fig. 2a validate that the model is not overfitted and the training ends after dozens of epochs. The optical sensing part of our converged model is presented in Fig. 2b. The resultant five diffractive layers mutually work to transform implicit OAM information into hierarchical features in the sensor plane. Note that these layers are not the same as those of Fig. 1 (trained with different hyperparameters and datasets), and the following test results are based on the system in Fig. 2b instead of Fig. 1. Inspired by the beam steering effect induced by phase gradients (e.g. a focus lens), we analyze the fifth layer's gradient values (Fig. 2b6) to straightforwardly show what exactly the diffractive layers are doing from the perspective of optics. In fact, as the structured light propagates and interacts with these layers consecutively, the spatial wavevectors are mixed sufficiently in an 'intelligent' manner that the light fields are redirected towards different regions of the sensor plane. We repeat the training phase several times under different hyperparameters and find that in most cases the incident optical field is transformed into speckle-like pattern, which contains high-dimensional sparse features related to TCs. Yet, an interesting case we obtain is the scheme sketched in Fig. 1: the optical part can 'split' the input beam into two main spatial lobes, where one lobe determines the OAM spectrum components with positive TCs and the other determines those with negative TCs (see Supplementary Video 1). This phenomenon indicates that our optical neural network is actually sensing the wavefront of structured field. In this way, our scheme

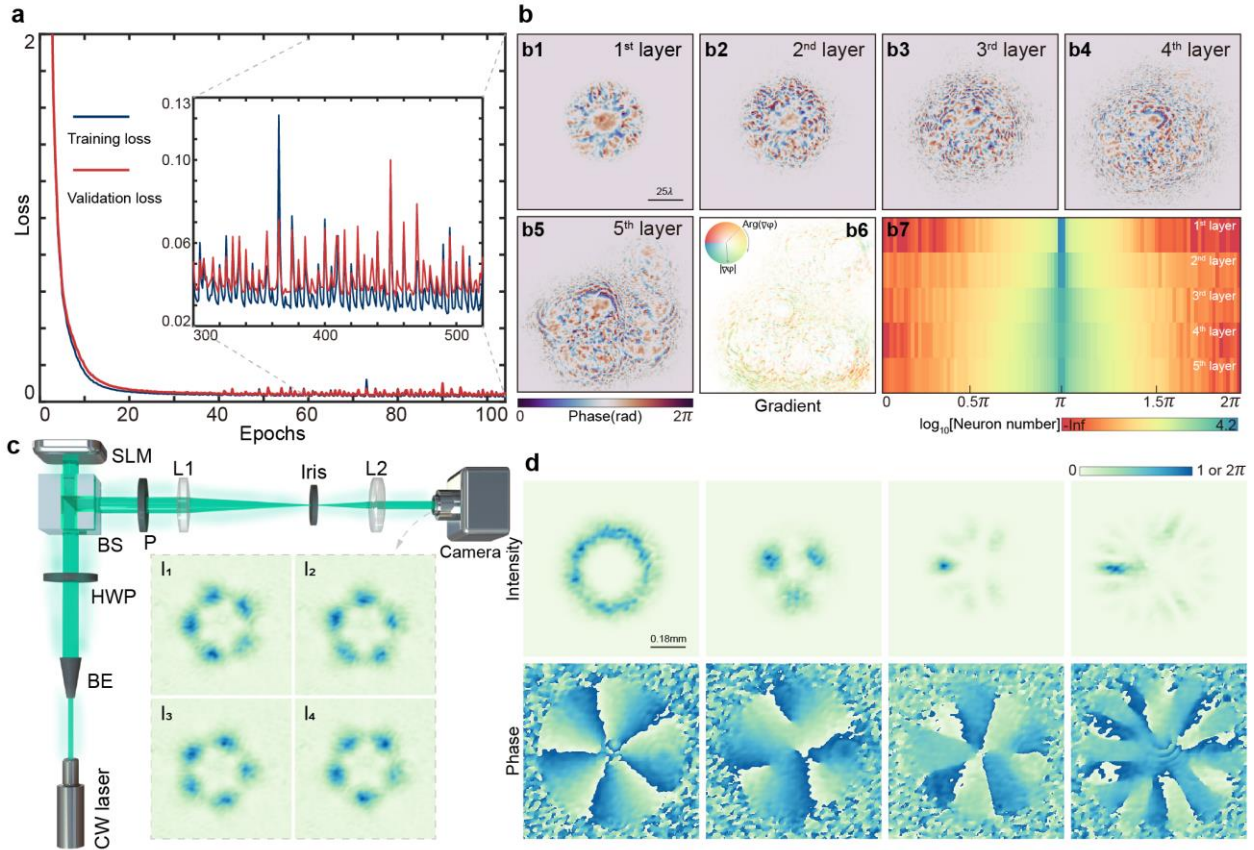


Fig. 2 Training results and experimental data collection. **a** The loss curves of training set and validation set versus updating epochs. The learning rate is tuned dynamically every 15 epochs. The POAM converges after dozens of epochs and the inset indicates that the neural network is not over-fitted. The loss value is the sum of 300 (one batch) samples. **b** Final designs of the optical diffractive neuron network. **b1** - **b5**: Five cascaded diffractive layers with a fixed distance of 40λ between two successive layers. **b6** The gradient distributions of the 5th layer. PS: Color-encoded gradient map. **b7** Phase value distributions of 5 diffractive layers, which reflect: 1) the interaction region between light and optical layer is expanding and 2) the optical neurons are sparse. **c** The optical setup for collecting experimental data. CW laser, continuous-wave laser; BE, beam expander; HWP, half-wave plate; BS, beam splitter; SLM, spatial light modulator; P, polarizer; L1, L2, lens. For each data sample, we reconstruct the complex optical fields using 4-step phase shift method as depicted in the inset (I_1 , I_2 , I_3 , I_4). See details in Methods. **d** Four selective reconstruction results based on **c**, which are single mode (TC = 5), multiplexed (mul.) mode (TC = -4, -1, equal weights), mul. mode (TC = -4, -3, 2, 5, equal weights), mul. mode (TC = -10 ~ 10, random weights), from left to right.

can naturally get rid of the misleading brought by degenerate intensity patterns, as confronted by earlier works using intensity-based DL recognition algorithms^{24, 25, 27, 47}.

Furthermore, we calculate the phase value distributions of the five neuron layers in Fig. 2b7. All these layers are initialized with constant value π . After training, though most phase values are close to π , especially for the first layer, the gradual trend from the 1st layer to the 5th layer reflects that the interaction region between the layer and local optical field expands bigger as the light goes deeper. This quantitative

observation not only indicates that the optical part is mixing the wavevectors towards the final target but also shows that the values of optical neurons are sparse (also see Supplementary Fig. S1 for sparse electronic weights). In neural network studies, parameter sparsity benefits the feature selection and model interpretability^{48,49}. In optics, this sparsity could manifest the convenience of physical fabrication/implementation of our engineered layers as well.

Next, we present numerical and experimental results from the POAMS for different tasks. To generate experimental structured light in our processor, we first reconstruct the complex optical fields through the 4-step phase shift method applying the experimental setup in Fig. 2c, which is also adopted in ref. ⁹ for OAM spectrum calculation (see Methods and Supplementary Note 1 for details and comparison). Some representative reconstruction results are depicted in Fig. 2d. We can clearly see the intensity and phase imperfections brought by nonideal laser source, possible astigmatism and distortion, sensor's noise, and other sources of error in our setup. Even so, the inference results from the processor are encouraging as we will exemplify in Fig. 3.

We first investigate the blind test performance on single vortex modes. We average the results from 30 repeated experiments and show them in Fig. 3a. The dominant diagonal values indicate that the hybrid processor outputs nearly perfect OAM spectra with experimental single modes input, only with a little deviation in Gaussian modes. Then the processor is employed to measure the OAM spectra of multiplexed OAM beams and two typical results based on 30 repeated experiments are illustrated in Fig. 3b, where sample 1 denotes multiplexed beam with equal weights and sample 2 represents beam with random weights at the OAM bases (see more in Supplementary Video 2). We can see a decent match between the output results and ground truths, even for very complicated OAM distributions. To further evaluate the measured results quantitatively, we calculate the R-squared (R^2) and mean squared error (MSE) values between the processor's outputs and corresponding ground truths, as shown in Fig. 3c. The average R^2 values for single modes, multiplexed modes with equal weights and random weights are 0.9924, 0.9268 and 0.8409, respectively, while the averaged MSE values are calculated as 3×10^{-4} , 5×10^{-4} , 2×10^{-4} respectively, validating the success of POAMS to detect OAM spectrum. Interestingly, the R^2 metric reveals that the model performs better on single modes while the MSE metric shows better results on multiplexed modes with random OAM weights. This can be partly explained by the better generalization performance, due to the fact that the MSE metric and simulated multiplexed modes are employed as the loss function and the training dataset. Beyond that, we find the hyperparameter temperature value T at the readout layer (see Methods, Eq. 8) can sharpen/smoothen the OAM output. For imperfect experimental single modes, the sharpening effect can mitigate the crosstalk to produce a near-perfect output as Fig. 3a. While for multiplexed modes, the sharpening effect may lead to a deteriorated OAM distribution. To further explore the influence of T , we train another 11 models with different T values (from 0.01 to 1, logspace, each model trained with 60 epochs) and present the averaged results upon different experimental datasets in Fig. 3d. Indeed, T can impact the convergence of the models as well as the final performance. With an optimized value e.g. $T \sim 10^{-1.2}$, one can achieve better results on multiplexed modes or single modes or mixture of them.

We emphasize that the generalization ability of POAMS is highly satisfactory. The applications of deep learning in optics are often hindered by the need of massive labelled experimental data to drive the update of the network parameters since the collection of experimental data in optics is typically impractical and

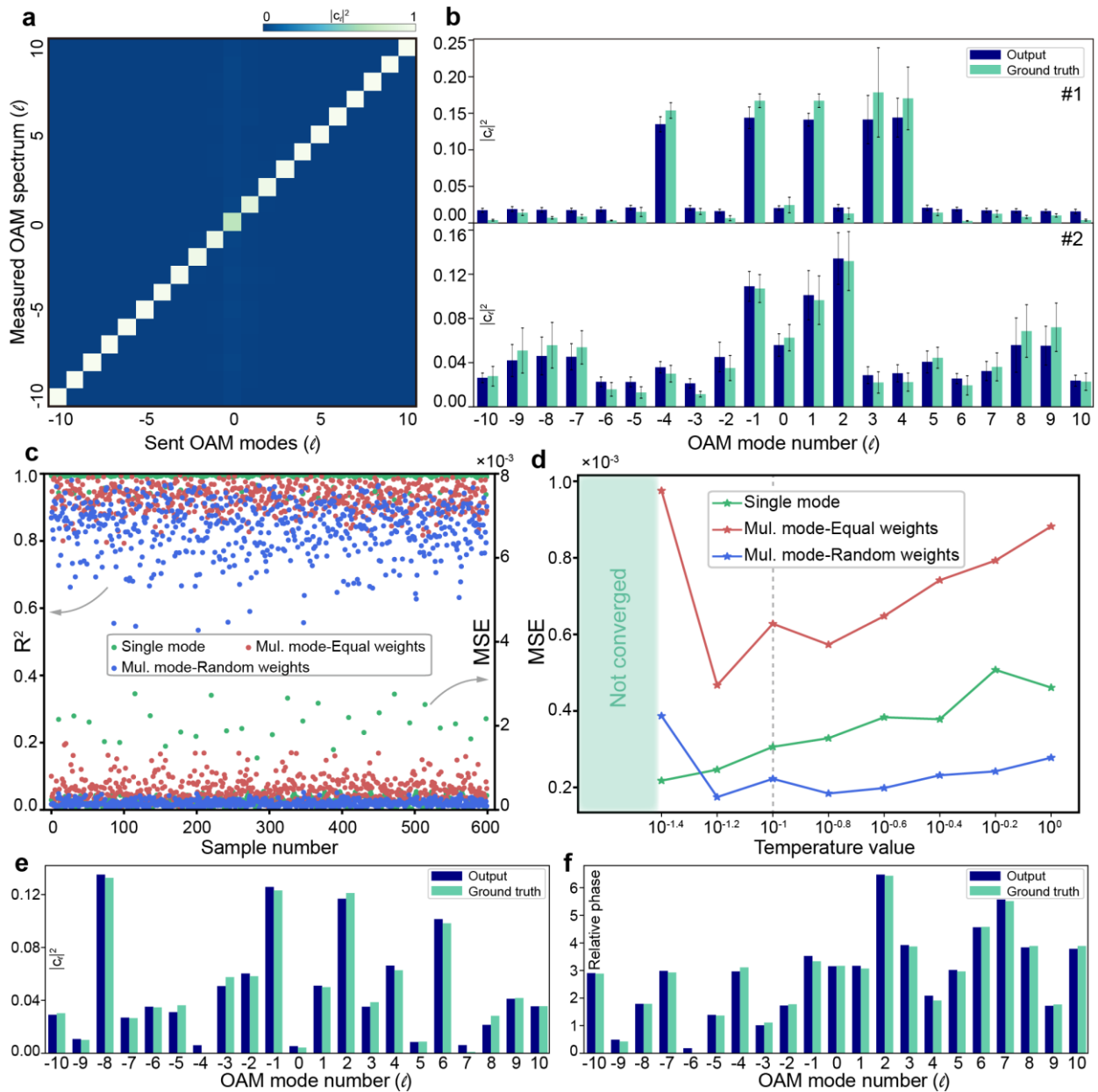


Fig. 3 OAM spectrum results for different structured light. **a** The results of experimental single modes with TC from -10 to 10 . Horizontal axis denotes different modes under test and longitudinal axis represents measured OAM spectrum. **b** Two selective results of experimental mul. modes. #1: mul. mode with equal weights. #2: mul. mode with random weights. Results of **a** and **b** are calculated based on 30 repeated experiments. Errorbar represents standard deviation. **c** Quantitative metrics to assess OAM spectrum measurement performance on different experimental datasets. Horizontal axis: index of each sample. R^2 : R-squared. MSE: mean squared error. **d** Model performance comparison on different datasets versus temperature value T . Each MSE value is calculated through the average on the whole experimental dataset. Each T corresponds to a trained model. The opaque cyan region means that the models with corresponding T values are not converged during training. The vertical gray line marks the model in Fig. 2a - b. **e - f** OAM complex spectrum on simulated mode. Left: weight. Right: relative phase.

prohibitively time consuming⁵⁰. However, in this work even the model is trained on a computer using ideal simulated dataset (only multiplexed modes with *random* OAM weights), the obtained processor is capable of predicting unseen *experimental single* modes and *multiplexed* modes with *equal* as well as *random* weights collected via the experimental scheme in Fig. 2c. This property is desirable for real-world communication applications by fast decoding various unknown OAM beams. We attribute the property to the inner wavefront sensing nature of the optical neural network, where the distortion of incident beam is acceptable as long as the global TC information hidden in phase is maintained.

In addition, as the complex spectrum (weight $|a_l|^2$ and relative intermodal phase ϕ_l) is reconstructed, the complete spatial information of target structured light can be attained for analyzing the in-depth optical properties (e.g. beam quality M^2 , wavefront at any longitudinal distance)^{10, 12}. We extend our processor to regress the OAM complex spectrum. This time we retrain a hybrid neural network with two parallel FCLs, which are responsible for the readouts of weights and relative phases respectively. Note the extension is rather implementable without losing the system's speed and energy advantages. The blind test results on simulated structured light are quite promising (Fig. 3e - f, obtained diffractive layers and more results are shown in Supplementary Video 3). The simulation results also inspire us that with an improved experimental system, our framework may achieve enhanced performance than those of Fig. 3a - c.

Robustness against several adverse effects. In realistic circumstances, incident structured light is prone to be distorted by many uncontrollable adverse factors. Consequently, pronounced channel crosstalk (or OAM redistribution) arises, which is detrimental for practical communication links^{2, 51, 52}. Therefore, the robustness of an OAM spectrum detection system is of great significance⁵³. Here, we analyze the robustness of the POAMS against five typical adverse conditions including transverse rotation (TR), transverse shift (TS), angular shift (AS), longitudinal shift (LS) and atmosphere turbulence (AT), as illustrated in the left panels of Fig. 4. The MSE metric is applied to gauge the performance through comparing the OAM spectra among ground truths *before* and *after* distortion (calculated by definition), and POAMS outputs.

A. Transverse rotation. It usually occurs when the detection module is indeliberately rotated. Additionally, as the optical layers in Fig. 1 and Fig. 2b possess no rotation symmetry, it's necessary to explore whether the POAMS is rotation-invariant. To exclude the influence of the inherent symmetry of incident beams, we use 20 multiplexed modes with random weights (intensity distribution: rotation-variant) rather than single modes (intensity distribution: rotation-invariant). As shown in Fig. 4a, when the transverse rotation angle varies from $-\pi$ to π , the averaged MSE values barely change ($\sim 10^{-5}$), implying that the POAMS can produce almost invariant spectra (see inset). Therefore, the POAMS exhibits strong robustness against TR.

B. Transverse shift & Angular shift. Another crucial factor is misalignment due to transverse and angular shift⁵⁴, as shown in left of Fig. 4b and c. It is an essential hurdle because it is unavoidable in realistic setups and it can induce distinct OAM spectrum changes⁵³. Here we analyze these two factors separately for simplicity. For generality, we average the output spectra for a given perturbation over 21 single modes. Owing to the TR robustness, it is reasonable to study TS varying from -1 to 1 (in beam width unit) and AS varying from -9.6×10^{-3} to 9.6×10^{-3} (in rad) only in xoz plane. The corresponding results are illustrated in right of Fig. 4b and c. The symmetric curves indicate identical performances. Taking Fig. 4b as an

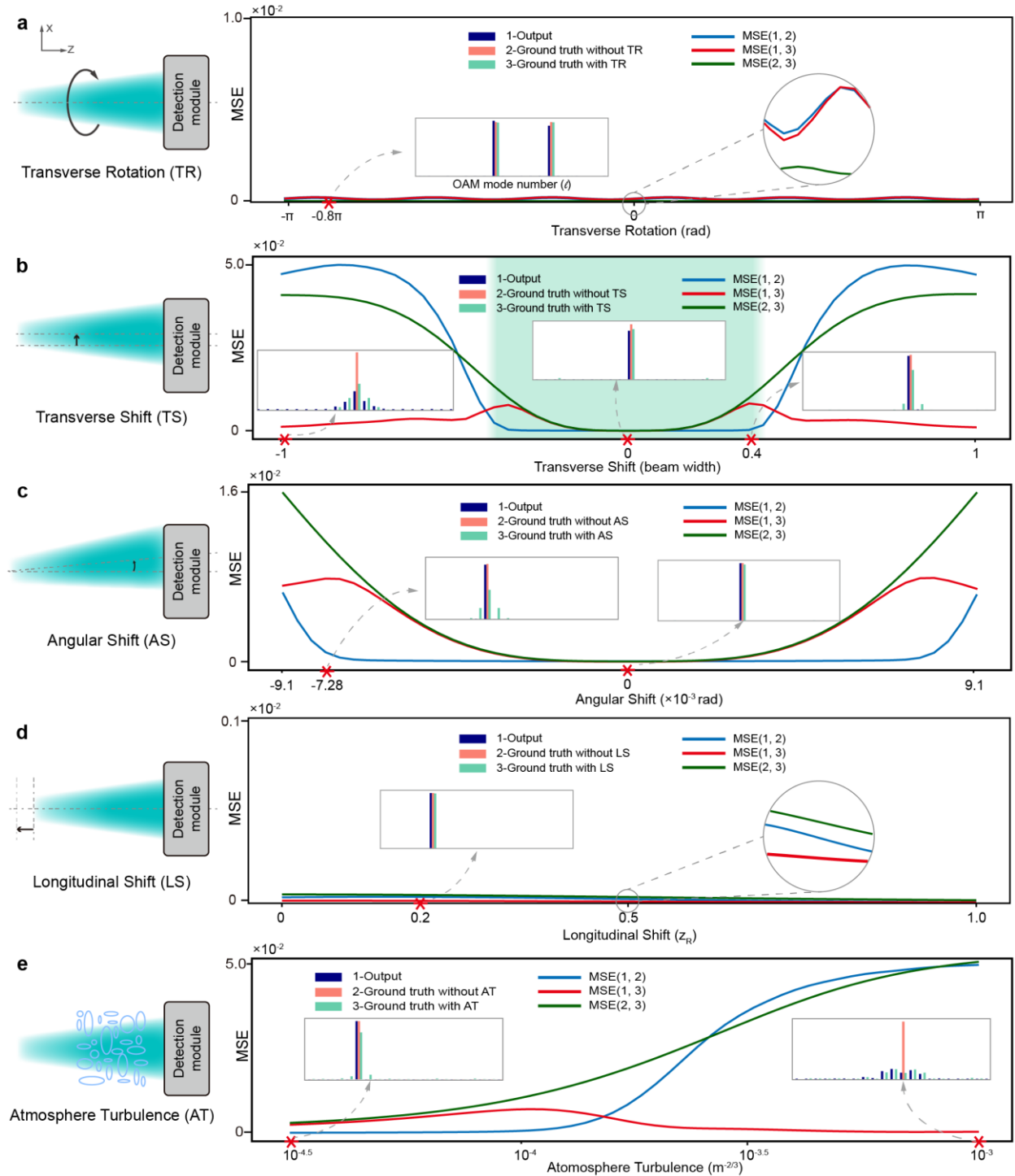


Fig. 4 Robustness analysis of the POAMS against adverse conditions. Left panel: schematic diagrams of different adverse conditions. In the right panel, blue curves represent the MSE values between POAMS outputs and ground truths before/without channel crosstalk. Red and green curves follow similar definitions. Inset: randomly selected OAM spectrum results (TC range: $-10 \sim 10$) under certain adverse conditions of **a** mul. mode (TC = $-2, 4$, equal weights), **b** single modes (TC = $0, 0, 1$), **c** single modes (TC = $-4, -2$), **d** single mode (TC = -5) and **e** single modes (TC = $-5, 1$). Note the fluctuations/gaps shown in the circled insets of **a** and **d** are trivial ($\sim 10^{-5}$). The opaque cyan region in **b** is obtained with reference to the flat part of the blue curve, which denotes the robustness range against TS. The robustness ranges in other subfigures can be similarly specified.

example, the flat range of the blue curve ($-0.4 \sim 0.4$ times beam width, also opaque cyan region) is significantly wider than that of green curve, which demonstrates that POAMS output spectra are closer to the ground truths without channel crosstalk. As the TS (AS) increases, the results of the POAMS tend to be in consistence with the ground truths after TS (AS).

C. Longitudinal shift. Without changing OAM spectrum, distance change between generation and detection module (i.e. longitudinal shift) will cause the deformation of incident wavefront induced by Gouy phase. Meanwhile, due to the divergence nature of propagating beams, LS also (de)magnifies beam width. As shown in Fig. 4d, by changing LS from 0 to $1.0 z_R$ (Rayleigh range), the output spectra maintain accurate, leading to distance-invariance of POAMS. It's mention-worthy that like any other optical systems, our model has an effective entrance pupil that can be observed from the interaction regions of the diffractive neural network as depicted in Fig. 2b1. When the incident beam width exceeds the regions, there may be no sufficient modulation and thus the processor loses efficacy.

D. Atmosphere turbulence. Besides the spatial imperfections, another critical factor that distorts the structured light during propagation is atmosphere turbulence (AT)⁵⁵. To demonstrate the corresponding robustness, we put the POAMS into different AT environments. Specifically, the modified von Karman model is employed to generate random phase plates, where the outer and inner scales of turbulence are set as 10 m and 0.01 m respectively. AT refractive index structure parameter C_n^2 varies from $10^{-4.5}$ to $10^{-3} \text{ m}^{-2/3}$ and five different phase plates are used to accumulate 500 m propagation distance in turbulence. As presented in Fig. 4e, the detection module (POAMS) can surprisingly mitigate the crosstalk under relatively weak AT, i.e. the output OAM spectra are very close to ground truths before distortion, even without any additional adaptive optics compensation techniques⁵⁶. For relatively strong AT, we obtain OAM spectra closer to the ground truths after distortion.

To sum up, the POAMS exhibits strong robustness against above five adverse effects from the intuitional curves (especially the blue curves) in Fig. 4. This robustness can further verify the wavefront sensing nature of the optical diffractive neural network. Namely our system is actually learning the *global* TC information hidden in phase structures rather than memorizing the *local* trivial features. The analysis of LS manifests a large tolerance of effective entrance pupil of the system, which benefits high efficiency and signal-to-noise ratio. As for TS, AS and AT, the POAMS behaves peculiarly under weak and strong distortions. In weak regimes, the POAMS suppresses the crosstalk hence the output OAM spectra remain unchanged. While in strong regimes, the results resemble OAM spectra with crosstalk. The former property can effectively improve the practicability of OAM-based communication links and the latter property can inspire novel applications of OAM beams, e.g. the POAMS could act as a novel sensor for fast AT prediction⁵⁷.

Model interpretation. A ubiquitous convolutional neural network (CNN) is composed of several convolutional layers for extracting high-dimensional features and FCLs for combining learned features (see Fig. 5a for architecture comparisons). Despite the popularity of CNN-enabled breakthroughs, a criticism is often raised against CNN on its 'black box' nature, i.e. it is hard to explain why a given input produces a corresponding output⁵⁸. On the other hand, clearly understanding how the neural networks work and what computations they perform can assist us to better improve the system. Otherwise, development of models is reduced to trial-and-error and misleading may arise without warning or explanation when models

collapse⁵⁹⁻⁶¹. To date, researchers have developed various techniques to visualize the CNN working principles e.g. t-SNE⁶², CAM⁶³, and Grad-CAM⁶⁰. Whereas, interpretation of hybrid optoelectronic neural networks still remains elusive. With the aid of optical diffraction theory³³ and previous visualization methods⁵⁹, here we propose a paradigm by: 1) analyzing the complex features behind each optical layer and 2) connecting the high-dimensional features in the sensor plane with the final OAM spectrum results.

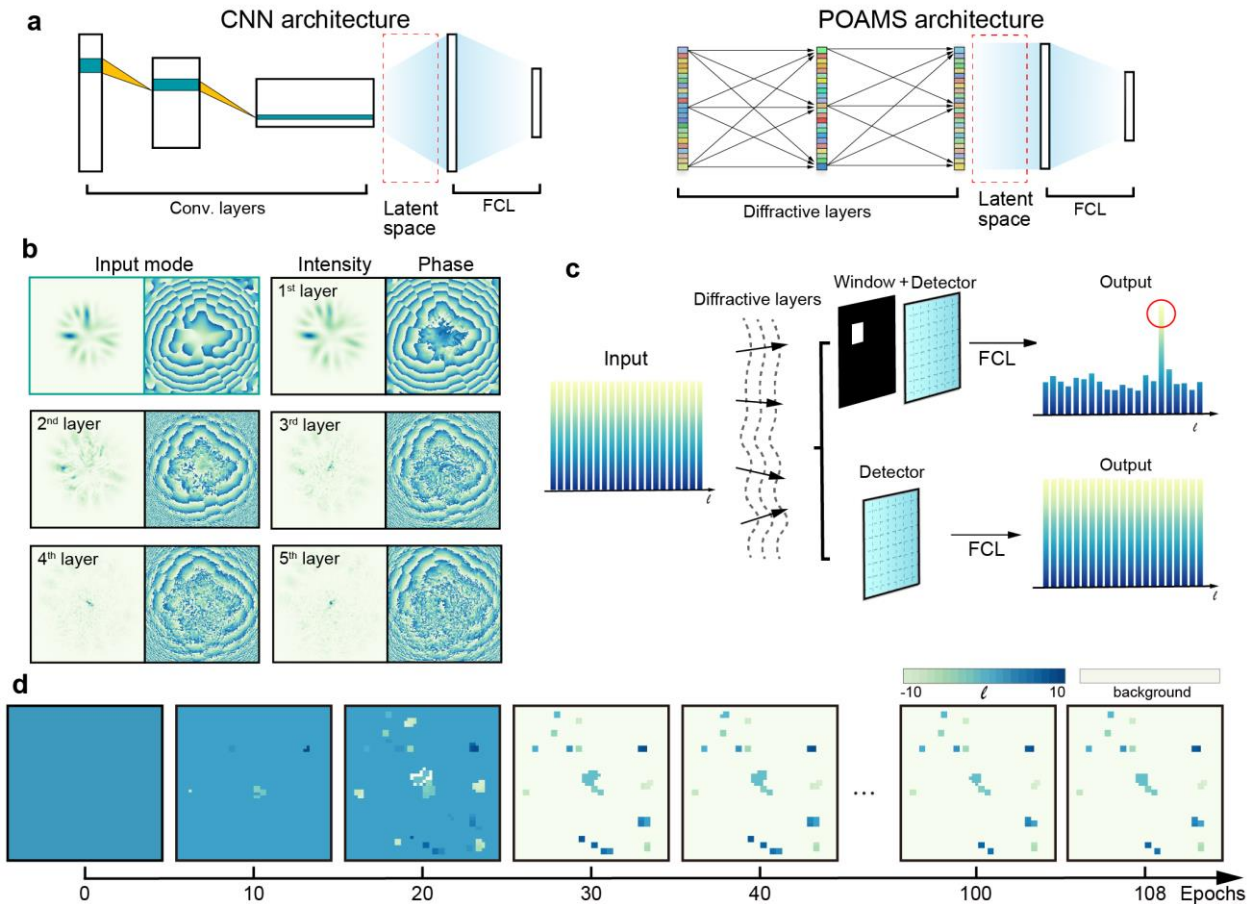


Fig 5 Visualization of the POAMS. **a** Architecture comparison between a conventional CNN (left) and the POAMS (right) for further model interpretation. The red dashed rectangles represent the latent space connecting electronic convolutional layers (or optical diffractive layers) and FCLs. **b** Visualization of the complex optical feature maps behind each diffractive layer. Intensity distributions are normalized. It can be straightforwardly seen that the diffractive layers can mix and redirect the spatial wavevectors ‘intelligently’. **c** The visualization workflow for searching the specific spatial regions in the detector plane that connects corresponding TC number. Window size (white box size): 2×2 . **d** Evolution of obtained characteristic graphs during training. Colormap encoded with TC number. Model at #108 epoch is the best model (with the lowest validation loss).

For the POAMS, we treat diffractive layers as CNN’s convolutional layers and also investigate the interaction between diffractive layer and readout layer. Specially, we firstly present complex optical fields behind each diffraction-modulation unit to see how the incident structured light is processed optically. Figure 5b elucidates the hierarchical features that the optical neural network is extracting. Though the features seem rambling to us, they are critical to the network. Stated differently, the blended TCs

information of structured light is transformed to easy-separable high-dimensional features in the latent space, so as to be globally regressed to model outputs. From our theoretical model (see Methods), the latent space in the detector plane plays a significant role in communicating complex optical signals with real electronic signals. On one hand, complex optical signals are turned to be real to provide greatly reduced parametric complexity and to enhance the accuracy of prediction. On the other hand, the compressed features enable us to interpret how each TC number connects to the spatial regions in the detector plane. Particularly, here we propose a method akin to prevailing occlusion sensitivity analysis in neural network studies⁵⁹, in accordance with the workflow in Fig. 5c and following steps:

- i) Utilize a window ahead of the detector which only leaks a portion of signals to flow into the readout layer and occludes others.
- ii) Monitor the consequence of OAM spectrum output and pick the OAM component which sticks out from others.
- iii) Repeat step ii) for 200 different input modes and decide one OAM component with maximum likelihood.
- iv) Slide the window with a fixed stride across the whole plane and repeat steps i), ii) and iii) to obtain a feature map.

Here, we define such map that identifies the connection between feature spatial regions and exact OAM components as the *characteristic graph*. Without occlusion, the model results show high consistency with ground truth. With a sliding window, we obtain such graphs shown in Fig. 5d. The characteristic graph exhibits several interesting properties. First, from the evolution of these graphs in Fig. 5d, the distribution converges after adequate training (~45 epochs) i.e. the general structure remains stable, only with tiny changes along evolution. Second, the distribution of the graph is globally invariant against the window size. Third, the graph tends to be complete during training, meaning that the graph contains all 21 OAM bases. More importantly, we find that once obtaining the graph, we are able to: 1) determine the existence of certain OAM component and 2) reconstruct the OAM spectra quite accurately, by only detecting the corresponding spatial regions at the graph. In other words, according to the graph, one can obtain the OAM information with much less scanning region and measurement steps when using single pixel detector (photodiode) or with much less detector size when using an array, which significantly improves detection efficiency by 25-fold (see details in Supplementary Note 3, Fig. S2 to S6).

In short, visualization of this model helps us better understand the interaction mechanisms between layers. Especially, we can determine which part of intensity signals in the detector plane contributes to certain OAM component. In this regard, the POAMS is significantly suitable for structured light detection by optically sensing corresponding wavefronts, extracting decisive features, decoupling the mixed TC information and electronically combining the global features to the final results. Compared to all-optical or all-electronic neural networks, the POAMS strikes a remarkable balance among model expressivity, inference speed and energy efficiency.

Discussion

The above results clearly show the exceptional power of the hybrid optoelectronic processor for OAM spectrum detection. First, the POAMS contains 0.2 million optical neurons and 5021 electronic neurons, leading to remarkable speed and energy efficiency. In other words, the optical-achieved 7.68×10^{10} computation operations cost little to no energy and are performed nearly at the speed of light, and electronic-achieved 1.26×10^7 operations cost relative low energy using a moderate computer. Then,

compared with existing OAM spectrum measurement methods, the POAMS conducts measurement in a direct single-shot manner, preventing the need of strict alignment for mode projection, reference wave for phase retrieval, etc. This, in one way, promises us a compact and elegant system (approximately $100\lambda \times 100\lambda \times 200\lambda$ with λ the working wavelength), and in another way, saves time and energy (see Supplementary Note 1 for details).

For the neural network convergence, despite fruitful discussions in all-optical D²NN training, the instructional analysis of hybrid optoelectronic neural networks is elusive⁴⁶, especially in terms of smooth and direct training pipeline. In this work, we find the imbalance between optical neurons and electronic neurons. Specifically, the gradient-descent-based algorithm updates the electronic neurons effectively while the optical parameters stay static, which hinders the successful updating of the joint model. By calculating the back propagation errors (see Methods), we introduce two hyperparameters to enhance the training efficiency, yielding a synchronized network parameter update.

The presented POAMS is scalable and can be further improved. For example, precisely detecting structured fields in the OAM basis over a wide wavelength range can be achieved utilizing this platform. Also, one can easily extend the OAM detection range by adjusting the number of neurons in the last layer, without compromising other advantages (see Supplementary Fig. S7 for POAMS performance on modes with out-of-range spectra). To advance the results reported in Fig. 3 and Fig. 4, one can scale up the training dataset by adding more data samples. Note we don't have to start from scratch to train the network, transfer learning technique⁶⁴ can be employed to fine-tune the POAMS. In this work, we limit our attention to scalar structured beams and the engineered diffractive layers are polarization-insensitive. Vectorial counterpart is also feasible⁶⁵, which could inspire efficient vector structured light detection. In addition to azimuthal mode spectrum this work discussed, crafting the POAMS into a radial mode spectrum can be relevant future work⁶⁶. Besides, the POAMS can be recognized as a solution to a regression problem in essence, and it could be extended to solve similar problems in other fields which necessities high speed and accuracy.

The free space propagation simulation is based on angular spectrum method with zero padding⁶⁷ so as to achieve results as convincing as possible. Indeed, the performance on unseen experimental data confirms the reliability of our processor. Regarding further implementation, the working wavelength is of decisive consideration. Recent advances have unlocked 3D printed layers in the terahertz spectral range⁶⁸, radio frequency range⁴⁴, and acoustic wave scheme⁴³, which are relatively large in size. But structured light is studied mostly in optical frequencies so the fabrication of optical neurons can be tricky. The multi-step photolithography-etching method can be considered⁴⁵.

In summary, we have demonstrated a compact optoelectronic processor for structured mode analysis, which can directly detect OAM spectrum of structured light in a fast, accurate and robust manner. Our processor allows one to immediately obtain the TC information without any interference measurements nor repetitive steps, empowered by the hybrid computing nature. We validate the performance on experimental and simulated structured modes with diverse (complex) OAM spectra and emphasize its robustness against nonideal conditions such as atmosphere turbulence, misalignment. In addition, we observe interesting connections between TC numbers and the optical neurons and consequently propose a model interpretation paradigm for hybrid neural networks, which not only help us understand the overall

system but also further improve the detection efficiency. This study highlights the advantages of fusing optics and electronics in settling photonics problems. More specifically, our approach closes a practical gap in OAM-based high-speed information processing and facilitates OAM and optoelectronic neural networks studies.

Methods

Forward propagation model. In addition to Eq. 2 and Fig. 1, here we provide a detailed illustration of the forward model. The optical computing part is based on the Rayleigh-Sommerfeld diffraction principles³³. Suppose there are M diffractive layers in the system and the vectorized output field after the modulation of the p th layer is denoted as E_p , $p = 1, 2, 3, \dots, M$, dimensions of which are $n^2 \times 1$ with n the neuron number along one direction of the layer. Then the complex transform between two modulation layers can be

$$E_p = \text{diag}(T_p) D_p E_{p-1}, \quad (4)$$

where $\text{diag}(\cdot)$ represents the diagonalization of a vector, $T_p = \alpha_p \exp(j\varphi_p)$ with $j^2 = -1$ is the modulation function and D_p is the diffraction weight matrix that is related with propagation distance and wavelength. Since in our case only phase modulation is employed, we set $\alpha_p \equiv \mathbf{1}$. We define $\varphi_p = \alpha\pi[\sin(\beta\theta_p) + 1]$, where $\sin(\cdot)$ function is to satisfy the periodicity condition of the argument and hyperparameters α and β are to facilitate the efficient update of these layers. Consequently, the output optical field in the sensor's plane is

$$E_{M+1} = D_{M+1} \left(\prod_{p=1}^M \text{diag}(T_p) D_p \right) E_0, \quad (5)$$

with E_0 the incident structured light. Then a sensor measures the intensity distribution of output field A_0 based on photoelectric effect, which also provides a quadratic nonlinear function and can be written as

$$A_0 = E_{M+1} \odot E_{M+1}^*, \quad (6)$$

where \odot is the Hadamard product and E_{M+1}^* represents the complex conjugate of output field. Then the high-dimensional sparse features of TC turn into real numbers and are entered as inputs of electronic readout layers. In our case, fully connected layers are used to regress the results. The weighted input value of q th layer can be formulated as

$$z_q = W_q A_{q-1} + B_q, \quad (7)$$

where $q = 1, 2, 3, \dots, N$, W_q is the weight matrix between two layers, A_{q-1} denotes the activation value of $(q-1)$ th layer, and B_q is the bias vector. We add nonlinear function $\sigma(\cdot)$ (Rectified Linear Units) into the electronic part and obtain activation value $A_{q-1} = \sigma(z_q)$. At the last layer, the neurons' input is $z_N = W_N A_{N-1} + B_N$. Considering that all weight components are non-negative and the sum of them must equal to 1, we adopt softmax(\cdot) function and a temperature parameter T to confine z_N ,

$$\hat{s} = \text{softmax}\left(\frac{z_N}{T}\right), \quad (8)$$

where \hat{s} is the OAM spectrum output (or A_N). Interestingly, T is a hyperparameter called temperature value that is normally set to 1 and a higher value leads to a softer probability distribution in knowledge distillation studies⁶⁹. Here we find that proper value of T can improve the robustness and performance of POAMS. In other words, proper temperature values (< 1) can successfully mitigate the channel crosstalk especially for single modes, due to the 'sharpening effect' T brings⁷⁰. Figure 3d clearly illustrates the influences of T on model performance.

Error Backpropagation. To effectively drive the update of POAMS parameters and minimize the loss

function $\mathcal{L}(s, \hat{s})$ in Eq. 3 of the main manuscript, we apply an error backpropagation algorithm. To implement this, we derive the key derivatives using the chain rule. First, we explore the derivatives of electronic layers and define the error at i th layer $\delta_i \equiv \partial \mathcal{L} / \partial \mathbf{z}_i$. Then the error in the output layer can be directly written as

$$\delta_L = \frac{\partial \mathcal{L}}{\partial \mathbf{A}_N} \odot \text{softmax}'(\mathbf{z}_N). \quad (9)$$

The error δ_q in terms of the error in the next layer δ_{q+1} can be derived as

$$\delta_q = (\mathbf{W}_{q+1}^T \delta_{q+1}) \odot \sigma'(\mathbf{z}_q). \quad (10)$$

By combining Eq. 9 with Eq. 10 we can calculate the error δ_q for any layer $(\delta_1, \delta_2, \dots, \delta_N)$. In this regard, the rate of change of the loss with respect to any weight and bias in the electronic layer can be obtained:

$$\begin{aligned} \frac{\partial \mathcal{L}}{\partial \mathbf{W}_q} &= \delta_q \mathbf{A}_{q-1}^T \\ \frac{\partial \mathcal{L}}{\partial \mathbf{B}_q} &= \delta_q \end{aligned} \quad (11)$$

For the optical neurons, we first calculate the error in the sensor plane,

$$\frac{\partial \mathcal{L}}{\partial \mathbf{A}_0} = \left(\frac{\partial \mathbf{z}_1}{\partial \mathbf{A}_0} \right)^T \frac{\partial \mathcal{L}}{\partial \mathbf{z}_1} = \mathbf{W}_1^T \delta_1. \quad (12)$$

Then to obtain the gradient of the p th diffractive layer, i.e.

$$\frac{\partial \mathcal{L}}{\partial \mathbf{T}_p} = \left(\frac{\partial \mathbf{A}_0}{\partial \mathbf{T}_p} \right)^T \frac{\partial \mathcal{L}}{\partial \mathbf{A}_0}, \quad (13)$$

we need to derive $\partial \mathbf{A}_0 / \partial \mathbf{T}_p$, which can be represented as

$$\begin{aligned} \frac{\partial \mathbf{A}_0}{\partial \mathbf{T}_p} &= \frac{\partial \mathbf{A}_0}{\partial \mathbf{E}_{M+1}} \frac{\partial \mathbf{E}_{M+1}}{\partial \mathbf{T}_p} + \frac{\partial \mathbf{A}_0}{\partial \mathbf{E}_{M+1}^*} \frac{\partial \mathbf{E}_{M+1}^*}{\partial \mathbf{T}_p}, \\ &= 2\text{Re} \left[\frac{\partial \mathbf{E}_{M+1}}{\partial \mathbf{T}_p} \text{diag}(\mathbf{E}_{M+1}^*) \right], \end{aligned} \quad (14)$$

where $\text{Re}(\cdot)$ denotes the operation of extracting the real part of complex values. Within Eq. 13, $\partial \mathbf{E}_{M+1} / \partial \mathbf{T}_p$ can be easily formulated as

$$\frac{\partial \mathbf{E}_{M+1}}{\partial \mathbf{T}_p} = \mathbf{D}_{M+1} \left(\prod_{i=M}^{p+1} \text{diag}(\mathbf{T}_i) \mathbf{D}_i \right) \mathbf{D}_p \text{diag}(\mathbf{E}_{p-1}). \quad (15)$$

Substituting Eq. 15 into Eq. 14 and Substituting Eq. 14 and Eq. 12 into Eq. 13, we have

$$\frac{\partial \mathcal{L}}{\partial \mathbf{T}_p} = \left\{ 2\text{Re} \left[\mathbf{D}_{M+1} \left(\prod_{i=M}^{p+1} \text{diag}(\mathbf{T}_i) \mathbf{D}_i \right) \mathbf{D}_p \text{diag}(\mathbf{E}_{p-1}) \text{diag}(\mathbf{E}_{M+1}^*) \right] \right\}^T \mathbf{W}_1^T \delta_1. \quad (16)$$

Considering that for POAMS, only phase modulation is applied, more specifically, $\mathbf{T}_p = \exp\{i\alpha\pi[\sin(\beta\theta_p) + 1]\}$, we are able to obtain the final gradient formula of optical parameters

$$\begin{aligned} \frac{\partial \mathcal{L}}{\partial \theta_p} &= \frac{\partial \mathbf{T}_p}{\partial \theta_p} \frac{\partial \mathcal{L}}{\partial \mathbf{T}_p} \\ &= \text{diag}\{\alpha\beta\pi\cos(\beta\theta_p)\} \text{diag}\{je^{j\alpha\pi[\sin(\beta\theta_p)+1]}\} \frac{\partial \mathcal{L}}{\partial \mathbf{T}_p}. \end{aligned} \quad (17)$$

In short, Eq. 11 and Eq. 17 represents the update of electronic neurons and optical neurons respectively. In the training phase, due to the nontrivial nonlinearity and mature training algorithms with respect to electronic neurons, the calculated errors and gradients can effectively optimize \mathbf{W}_q and \mathbf{B}_q . However, the backpropagated errors cannot update θ_p efficiently. To address this hurdle, we introduce α and β to enhance the corresponding gradients as indicated in Eq. 17 and yield the successful refreshment of the overall system.

Dataset acquisition and processing. To train the POAMS, we prepare a dataset with 500 distinct OAM spectra. We use supervised learning technique to update the network. Each structured light is generated by superposing 21 OAM eigenmodes (TC, $-10 \sim 10$) and normalized as network input. And the corresponding label is generated randomly using `normrnd` function in Matlab (MathWorks Inc.). To augment the dataset, each structured light with a specific weight label is endowed with 50 different intermodal phase distributions (generated using `randn` function), leading to a dataset with $500 \times 50 = 25000$ samples. To conduct the model interpretation experiment of Fig. 5, we also add another 2000 samples with identical uniform OAM spectrum into the training set. Similarly we generate 5000 samples each for further validation and test.

To test the POAMS, we also collect experimental data samples using the scheme in Fig. 2c. We apply a 532 nm continuous-wave laser (CNI laser, MGL-III-532) as the light source. The beam is expanded through a telescope, linearly polarized through a half wave plate and then directed onto the spatial light modulator (Hamamatsu, X13138-04, pixel size of $12.5 \mu\text{m}$, resolution of 1280×1024). Then the modulated beam is projected onto the camera (AVT Mako G-131B, pixel size of $5.3 \mu\text{m}$, resolution of 1280×1024) plane through a 4-f system, in which the first diffraction order target beam is filtered out via an iris. We then reconstruct the complex optical field applying the 4-step phase shift method. This method requires a reference wave, which is assumed as plane wave $E_R = A_R$. To obtain the signal $E_S = A_S \exp(j\phi_S)$, we measure the intensity distribution at least for 4 times, i.e. $I_i = |E_S e^{j(i-1)\pi/2}|^2$, $i = 0, 1, 2, 3$. The final result can be easily derived as

$$E_S = \frac{I_1 - I_3}{4A_R} + j \frac{I_4 - I_2}{4A_R}. \quad (18)$$

In fact, A_R also needs to be recorded in experiments so there are 5 overall repetitive measurements. By doing so, we are able to let the experimental structured light propagate in the POAMS. Note the experimental OAM spectrum label is calculated through the definition/method in ref. ⁹. The label acquisition process also reflects the simplicity and elegance of our POAMS. To validate the generalization ability of the POAMS, we collect diverse data samples through this scheme covering structured light with single OAM spectrum, equally multiplexed OAM spectrum, and randomly multiplexed OAM spectrum, which were all different from the training set and not seen by the POAMS. To match the POAMS input size, once we obtain the raw data of intensity distributions from the camera, all images are cropped to 600×600 pixel regions and then downsampled to 200×200 pixel regions through a bicubic method. Then all the intensity images are smoothed with a Gaussian filter before complex optical fields reconstruction.

Acknowledgements

This work is funded by the National Natural Science Foundation of China (61975087).

Author contributions

H.W. and Z.Z. conceived the original idea, developed the theory, conducted the experiment, analyzed the data and prepared the manuscript with input from all authors. Q.L. and X.F. supervised the project. All authors provided critical feedback and helped shape the research.

Data availability

The datasets and codes for this study are available from the corresponding authors upon reasonable

request.

Conflict of interest

The authors declare no competing interests.

References

1. Allen, L., Beijersbergen, M.W., Spreeuw, R.J.C., Woerdman, J.P. Orbital angular momentum of light and the transformation of Laguerre-Gaussian laser modes. *Phys. Rev. A* **45**, 8185-8189 (1992).
2. Willner, A.E., Pang, K., Song, H., Zou, K., Zhou, H. Orbital angular momentum of light for communications. *Appl. Phys. Rev.* **8**, 041312 (2021).
3. Yuanjie, Y., Yuxuan, R., Mingzhou, C., Yoshihiko, A., Carmelo, R.-G. Optical trapping with structured light: a review. *Adv. Photonics* **3** (2021).
4. Erhard, M., Fickler, R., Krenn, M., Zeilinger, A. Twisted photons: new quantum perspectives in high dimensions. *Light Sci. Appl.* **7**, 17146-17146 (2018).
5. Xie, Z. et al. Ultra-broadband on-chip twisted light emitter for optical communications. *Light Sci. Appl.* **7**, 18001-18001 (2018).
6. Hickmann, J.M., Fonseca, E.J.S., Soares, W.C., Chávez-Cerda, S. Unveiling a Truncated Optical Lattice Associated with a Triangular Aperture Using Light's Orbital Angular Momentum. *Phys. Rev. Lett.* **105**, 053904 (2010).
7. Wen, Y. et al. Spiral Transformation for High-Resolution and Efficient Sorting of Optical Vortex Modes. *Phys. Rev. Lett.* **120**, 193904 (2018).
8. Grillo, V. et al. Measuring the orbital angular momentum spectrum of an electron beam. *Nat. Commun.* **8**, 15536 (2017).
9. Fu, S. et al. Universal orbital angular momentum spectrum analyzer for beams. *Photonix* **1**, 19 (2020).
10. D'Errico, A., D'Amelio, R., Piccirillo, B., Cardano, F., Marrucci, L. Measuring the complex orbital angular momentum spectrum and spatial mode decomposition of structured light beams. *Optica* **4**, 1350-1357 (2017).
11. Forbes, A., Dudley, A., McLaren, M. Creation and detection of optical modes with spatial light modulators. *Adv. Opt. Photonics* **8**, 200-227 (2016).
12. Zhou, H.-L. et al. Orbital angular momentum complex spectrum analyzer for vortex light based on the rotational Doppler effect. *Light Sci. Appl.* **6**, e16251-e16251 (2017).
13. Malik, M. et al. Direct measurement of a 27-dimensional orbital-angular-momentum state vector. *Nat. Commun.* **5**, 3115 (2014).
14. Chen, P. et al. Digitalizing Self-Assembled Chiral Superstructures for Optical Vortex Processing. *Adv. Mater.* **30** (2018).
15. LeCun, Y., Bengio, Y., Hinton, G. Deep learning. *Nature* **521**, 436-444 (2015).
16. Eraslan, G., Avsec, Ž., Gagneur, J., Theis, F.J. Deep learning: new computational modelling techniques for genomics. *Nat. Rev. Genet.* **20**, 389-403 (2019).
17. Elmarakeby, H.A. et al. Biologically informed deep neural network for prostate cancer discovery. *Nature* **598**, 348-352 (2021).
18. Lu, L., Jin, P., Pang, G., Zhang, Z., Karniadakis, G.E. Learning nonlinear operators via DeepONet based on the universal approximation theorem of operators. *Nat. Mach. Intell.* **3**, 218-229 (2021).
19. Fang, L. et al. Deep learning-based point-scanning super-resolution imaging. *Nat. Methods* **18**, 406-416 (2021).

20. Shi, L., Li, B., Kim, C., Kellnhofer, P., Matusik, W. Towards real-time photorealistic 3D holography with deep neural networks. *Nature* **591**, 234-239 (2021).
21. Genty, G. et al. Machine learning and applications in ultrafast photonics. *Nat. Photonics* **15**, 91-101 (2021).
22. Jiang, J., Chen, M., Fan, J.A. Deep neural networks for the evaluation and design of photonic devices. *Nat. Rev. Mater.* **6**, 679-700 (2021).
23. Zuo, C. et al. Deep learning in optical metrology: a review. *Light Sci. Appl.* **11**, 39 (2022).
24. Giordani, T. et al. Machine Learning-Based Classification of Vector Vortex Beams. *Phys. Rev. Lett.* **124**, 160401 (2020).
25. Liu, Z., Yan, S., Liu, H., Chen, X. Superhigh-Resolution Recognition of Optical Vortex Modes Assisted by a Deep-Learning Method. *Phys. Rev. Lett.* **123**, 183902 (2019).
26. Wang, H. et al. Deep-learning-based recognition of multi-singularity structured light. *Nanophotonics* **11**, 779-786 (2022).
27. Feng, F. et al. Deep Learning-Enabled Orbital Angular Momentum-Based Information Encryption Transmission. *ACS Photonics* (2022).
28. He, K., Zhang, X., Ren, S., Sun, J. in 2016 IEEE Conference on Computer Vision and Pattern Recognition (CVPR) 770-778 (2016).
29. Wetzstein, G. et al. Inference in artificial intelligence with deep optics and photonics. *Nature* **588**, 39-47 (2020).
30. Shastri, B.J. et al. Photonics for artificial intelligence and neuromorphic computing. *Nat. Photonics* **15**, 102-114 (2021).
31. Zhou, H. et al. Photonic matrix multiplication lights up photonic accelerator and beyond. *Light Sci. Appl.* **11**, 30 (2022).
32. Shen, Y. et al. Deep learning with coherent nanophotonic circuits. *Nat. Photonics* **11**, 441-446 (2017).
33. Lin, X. et al. All-optical machine learning using diffractive deep neural networks. *Science* **361**, 1004-1008 (2018).
34. Feldmann, J. et al. Parallel convolutional processing using an integrated photonic tensor core. *Nature* **589**, 52-58 (2021).
35. Rafayelyan, M., Dong, J., Tan, Y., Krzakala, F., Gigan, S. Large-Scale Optical Reservoir Computing for Spatiotemporal Chaotic Systems Prediction. *Phys. Rev. X* **10**, 041037 (2020).
36. Wright, L.G. et al. Deep physical neural networks trained with backpropagation. *Nature* **601**, 549-555 (2022).
37. Kulce, O., Mengü, D., Rivenson, Y., Ozcan, A. All-optical information-processing capacity of diffractive surfaces. *Light Sci. Appl.* **10**, 25 (2021).
38. Zhou, T. et al. Large-scale neuromorphic optoelectronic computing with a reconfigurable diffractive processing unit. *Nat. Photonics* **15**, 367-373 (2021).
39. Luo, Y. et al. Computational imaging without a computer: seeing through random diffusers at the speed of light. *eLight* **2**, 4 (2022).
40. Veli, M. et al. Terahertz pulse shaping using diffractive surfaces. *Nat. Commun.* **12**, 37 (2021).
41. Qian, C. et al. Performing optical logic operations by a diffractive neural network. *Light Sci. Appl.* **9**, 59 (2020).
42. Goi, E. et al. Nanoprinted high-neuron-density optical linear perceptrons performing near-infrared inference on a CMOS chip. *Light Sci. Appl.* **10**, 40 (2021).
43. Weng, J. et al. Meta-neural-network for real-time and passive deep-learning-based object recognition.

- Nat. Commun.* **11**, 6309 (2020).
44. Liu, C. et al. A programmable diffractive deep neural network based on a digital-coding metasurface array. *Nat. Electron.* **5**, 113-122 (2022).
 45. Chen, H. et al. Diffractive Deep Neural Networks at Visible Wavelengths. *Engineering* **7**, 1483-1491 (2021).
 46. Mengü, D., Luo, Y., Rivenson, Y., Ozcan, A. Analysis of Diffractive Optical Neural Networks and Their Integration With Electronic Neural Networks. *IEEE J SEL TOP QUANT* **26**, 1-14 (2020).
 47. Wang, Z. et al. Recognizing the orbital angular momentum (OAM) of vortex beams from speckle patterns. *Sci. China Phys. Mech. Astron.* **65**, 244211 (2022).
 48. Venkatesh, B., Anuradha, J. A Review of Feature Selection and Its Methods. *Cybern. Inf. Technol.* **19**, 3-26 (2019).
 49. Zhou, Z.-H. *Machine Learning*. (Springer, Singapore; 2021).
 50. Li, J. et al. Deep learning-based quantitative optoacoustic tomography of deep tissues in the absence of labeled experimental data. *Optica* **9**, 32-41 (2022).
 51. Shen, Y. et al. Optical vortices 30 years on: OAM manipulation from topological charge to multiple singularities. *Light Sci. Appl.* **8**, 90 (2019).
 52. Lei, T. et al. Massive individual orbital angular momentum channels for multiplexing enabled by Dammann gratings. *Light Sci. Appl.* **4**, e257-e257 (2015).
 53. Wang, X. et al. Learning to recognize misaligned hyperfine orbital angular momentum modes. *Photonics Res.* **9**, B81-B86 (2021).
 54. Lin, J., Yuan, X.C., Chen, M., Dainty, J.C. Application of orbital angular momentum to simultaneous determination of tilt and lateral displacement of a misaligned laser beam. *J. Opt. Soc. Am. A* **27**, 2337-2343 (2010).
 55. Fu, S., Gao, C. Influences of atmospheric turbulence effects on the orbital angular momentum spectra of vortex beams. *Photonics Res.* **4**, B1-B4 (2016).
 56. Ren, Y. et al. Adaptive-optics-based simultaneous pre- and post-turbulence compensation of multiple orbital-angular-momentum beams in a bidirectional free-space optical link. *Optica* **1**, 376-382 (2014).
 57. Lavery, M.P.J., Chen, Z., Cheng, M., McKee, D., Yao, A. in *Society of Photo-Optical Instrumentation Engineers (SPIE) Conference Series*, Vol. 11926 1192611 (2021).
 58. Huff, D.T., Weisman, A.J., Jeraj, R. Interpretation and visualization techniques for deep learning models in medical imaging. *Phys. Med. Biol.* **66**, 04TR01 (2021).
 59. Zeiler, M.D., Fergus, R. in *Computer Vision – ECCV 2014*. (eds. D. Fleet, T. Pajdla, B. Schiele & T. Tuytelaars) 818-833 (Springer International Publishing, Cham; 2014).
 60. Selvaraju, R.R. et al. Grad-CAM: Visual Explanations from Deep Networks via Gradient-Based Localization. *Int J Comput Vis* **128**, 336-359 (2020).
 61. Yosinski, J., Clune, J., Nguyen, A., Fuchs, T., Lipson, H. Understanding Neural Networks Through Deep Visualization. arXiv:1506.06579 (2015).
 62. Laurens, V.D.M., Hinton, G.J.J.o.M.L.R. Visualizing Data using t-SNE. *J Mach Learn Res* **9**, 2579-2605 (2008).
 63. Zhou, B., Khosla, A., Lapedriza, A., Oliva, A., Torralba, A. in *2016 IEEE Conference on Computer Vision and Pattern Recognition (CVPR)* 2921-2929 (2016).
 64. Zhuang, F. et al. A Comprehensive Survey on Transfer Learning. *Proc. IEEE* **109**, 43-76 (2021).
 65. Luo, X. et al. Metasurface-Enabled On-Chip Multiplexed Diffractive Neural Networks in the Visible. arXiv:2107.07873 (2021).

66. Zhou, Y. et al. Sorting Photons by Radial Quantum Number. *Phys. Rev. Lett.* **119**, 263602 (2017).
67. Matsushima, K., Shimobaba, T. Band-Limited Angular Spectrum Method for Numerical Simulation of Free-Space Propagation in Far and Near Fields. *Opt. Express* **17**, 19662-19673 (2009).
68. Luo, Y. et al. Design of task-specific optical systems using broadband diffractive neural networks. *Light Sci. Appl.* **8**, 112 (2019).
69. Hinton, G., Vinyals, O., Dean, J. Distilling the Knowledge in a Neural Network. arXiv:1503.02531 (2015).
70. Berthelot, D. et al. MixMatch: A Holistic Approach to Semi-Supervised Learning. arXiv:1905.02249 (2019).